CHAPTER V

DEVELOPMENT OF A GOLD NANOPARTICLE-BASED NOVEL DIAGNOSTIC PROTOTYPE FOR *in vivo* DETECTION OF INDIAN RED SCORPION (*Mesobuthus tamulus*) VENOM

5.1 Results

5.1.1 Custom peptides (CPs) designed from major toxins of *Mesobuthus tamulus*

The predominant toxins of *Mesobuthus tamulus* venom (MTV), the antigenic regions of these toxins, and the CPs designed from these antigenic epitopes have been summarised in Table 5.1.

Table 5.1 The antigenic epitopes and the antigenic propensity of the native and modified epitopes are predominant toxins in the MTV proteome.

Name of toxin	**Antigenic epitope(s)**	**The antigenic propensity of toxin epitopes**	**Epitope-based synthetic peptides. Modified residues are underlined, and the length of the peptide is shown in parenthesis**	**Designation of custom peptide**	**The antigenic propensity of modified peptides**
Na^+ channel toxin (α-neurotoxin)	^{36}CDWWVPYGVVCWCEDLPTPVPIR^{58}	1.1089	CWWVPYGVVSWSEDLPTPVP (20)	CPS1	1.0907
	^{12}CTYICTFNNYCHALCTD^{28}	1.1045	YISTFNNYSHALSTDC (16)	CPS2	1.0418
K^+ channel toxin (Tamapin)	^{4}NLRRCELSCRSLGLLGKC^{21}	1.0797	SNLRRSELSSRSLGLLGKC (19)	CPS3	1.0340
	^{4}DVKCISSQECWIACKKV^{20}	1.1064	DVKSISSQESWIASKKVC (18)	CPS4	1.0567

Polyclonal antibodies against KLH-conjugated CPs were raised in rabbits and affinity purified. A high titre of antibodies was observed in rabbit sera (Fig. 5.1a-d). The purified antibodies did not show recognition towards the KLH carrier protein.

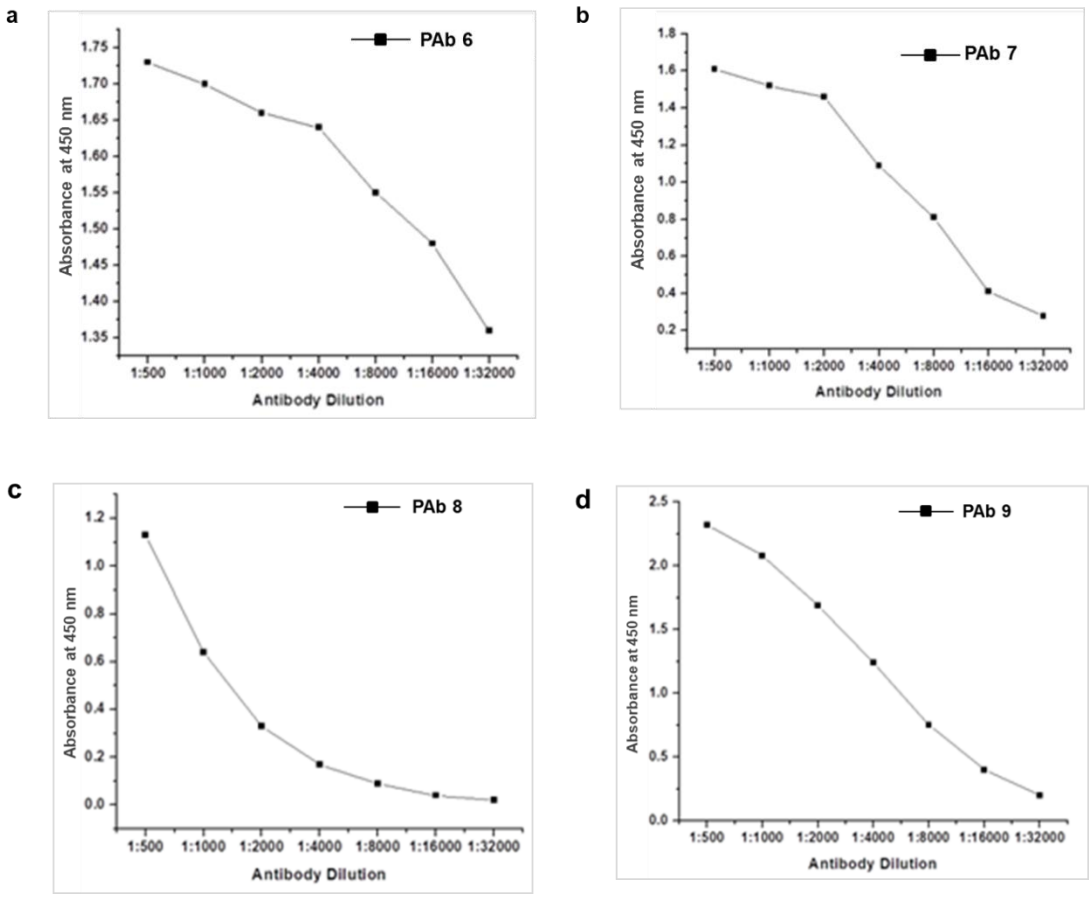

Fig. 5.1 Determination of titer of purified antibody by ELISA: **(a)** PAb 6, **(b)** PAb 7, **(c)** PAb 8, and **(d)** PAb 9.

5.1.1.1 Dot blot study demonstrated ability of PAbs to recognize CPs

The PAbs could recognise the CPs against which they were raised to varying degrees under identical experimental conditions (Fig. 5.1e, f). However, cross-reactivity among CPs and PAbs could not be observed.

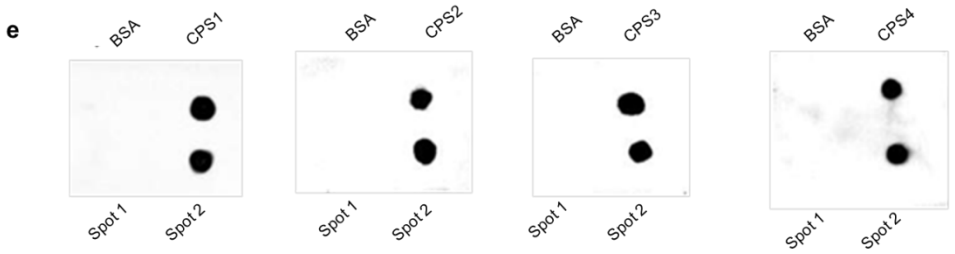

f

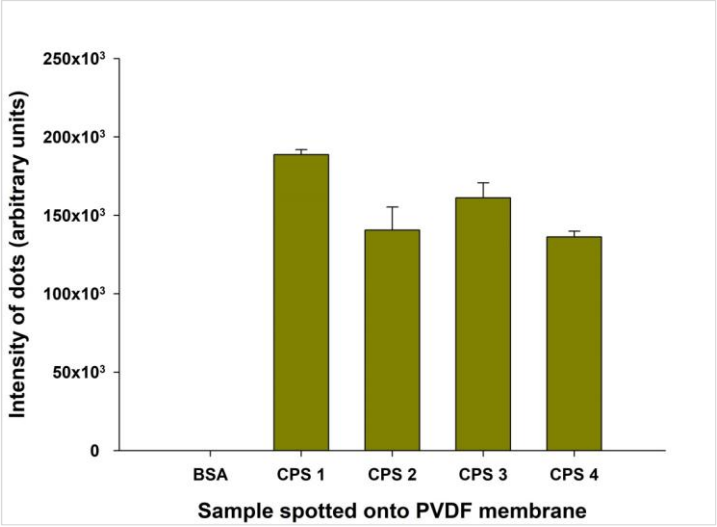

Fig. 5.1 (e) Immune recognition of the individual purified PAbs towards the respective CPs by dot blot assay; **(f)** Image analyses of dot intensities of immune reactivity depicted by the PAbs. CPS 1, 2, 3 and 4 denotes custom peptide 1, 2, 3 and 4. Error bars indicate mean ± S.D (n=3).

5.1.2 Immunoassays and spectrofluorometric analysis exhibit superior immune recognition of PAbF towards MTV as compared to commercial ASA (*in vitro*)

Indirect ELISA demonstrated that the PAbs raised against PAb 8 showed significantly higher immune cross-reactivity than the PAbs raised against PAb 6, 7, and 9, towards 100 ng MTV (Fig. 5.2a). The optimum immune cross-reactivity of PAb 8 was observed at a ratio of 1:40 (MTV: PAb), after which a saturation in immune cross-reactivity was observed (Fig. 5.2a). However, the immune cross-reactivity values of PAbs 6, 7, and 9 towards MTV did not differ significantly.

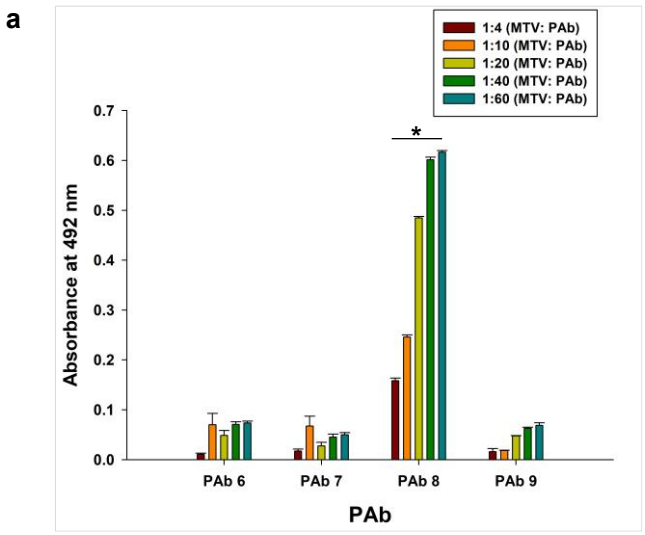

Fig. 5.2 (a) Immune-reactivity of the individual PAbs towards MTV, at 1:4, 1:10, 1:20, 1:40, and 1:60 (MTV: PAb) determined by Indirect ELISA. Significance of difference of recognition by PAb 6, 7, and 9 (1:4, 1:10, 1:20, 1:40, 1:60, MTV: PAb) compared to PAb 8, $^{*}p<0.05$. Error bars indicate mean ± S.D. (n=3).

In the subsequent phase, we examined the effect of various formulations of PAbs on the recognizing MTV. The PAbF exhibited markedly superior MTV recognition efficacy ($p<0.05$) vs to the individual PAbs and other PAb formulations (Fig. 5.2b).

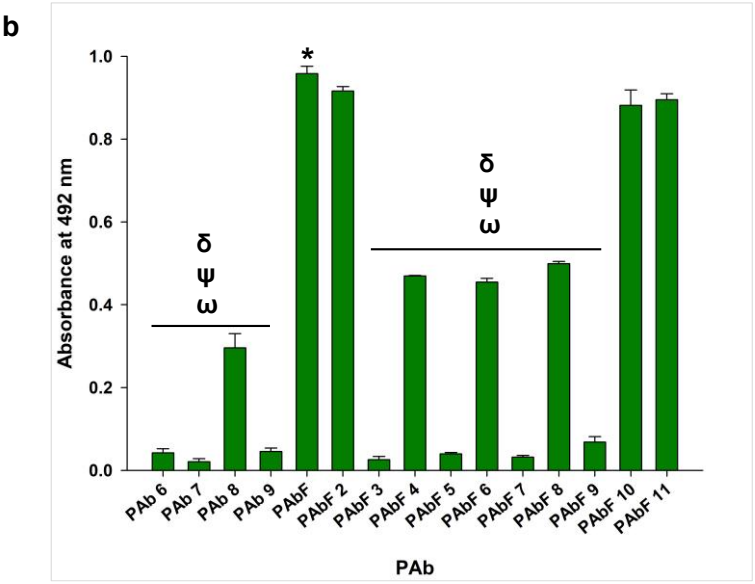

Fig. 5.2 (b) Comparison of the immune cross-reactivity of the four PAbs individually and in different combinations towards MTV at 1:40 (MTV: PAb) determined by Indirect ELISA. Significance of difference of MTV immune-recognition by PAb

individual and PAbF 2,3,4,5,6,7,8,9,10 and 11 compared to PAbF, *p<0.05; MTV immune-recognition by PAb individual and PAbF 3,4,5,6,7,8 and 9 compared to PAbF 2, $^{\delta}$p<0.05; MTV immune-recognition by PAb individual, PAbF 3,4,5,6,7,8 and 9 compared to PAbF 10, $^{\psi}$p<0.05; MTV immune-recognition by PAb individual, PAbF 3,4,5,6,7,8 and 9 compared to PAbF 11, $^{\omega}$p<0.05. Error bars indicate mean ± S.D (n=3).

[PAbF 2 denotes PAb 6+7+8+9 (1:1:1:1, w/w/w/w), PAbF 3 denotes PAb 6+7 (1:1, w/w), PAbF 4 denotes PAb 6+8 (1:1, w/w), PAbF 5 denotes PAb 6+9 (1:1, w/w), PAbF 6 denotes PAb 7+8 (1:1, w/w), PAbF 7 denotes PAb 7+9 (1:1, w/w), PAbF 8 denotes PAb 8+9 (1:1, w/w), PAbF 9 denotes PAb 6+7+9 (1:1:1, w/w/w), PAbF 10 denotes PAb 8+9+6 (1:1:1, w/w/w) and PAbF 11 denotes PAb 8+9+7 (1:1:1, w/w/w)].

The dose-dependent ELISA demonstrated that the PAbF could recognise MTV even at a low dose of 6.25 ng (Fig. 5.2c). Moreover, PAbF showed about 3-8 fold higher immune cross-reactivity (p<0.05) than that of the commercial ASA towards MTV under identical experimental conditions (Fig. 5.2c).

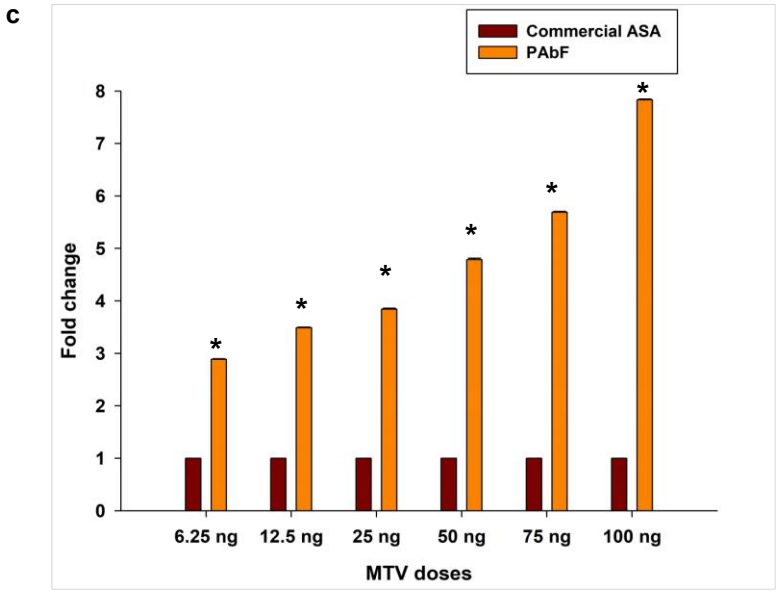

Fig. 5.2 (c) Comparison of the immune cross-reactivity between PAbF/ commercial ASA towards MTV determined by Indirect ELISA. There is a significant difference in the fold change value between the immune-reactivity of commercial ASA and PAbF at all the MTV doses, *p < 0.05.

As we are using the same antibody for both capture and detection, we performed a dot blot assay where it was observed that the secondary antibody (anti-rabbit IgG-

HRP/anti-horse IgG-HRP) showed weaker immune-recognition towards the capture antibody (dot intensities designated as control without antigen) (Fig. 5.2d, e); these blots have been called control without antigen henceforth.

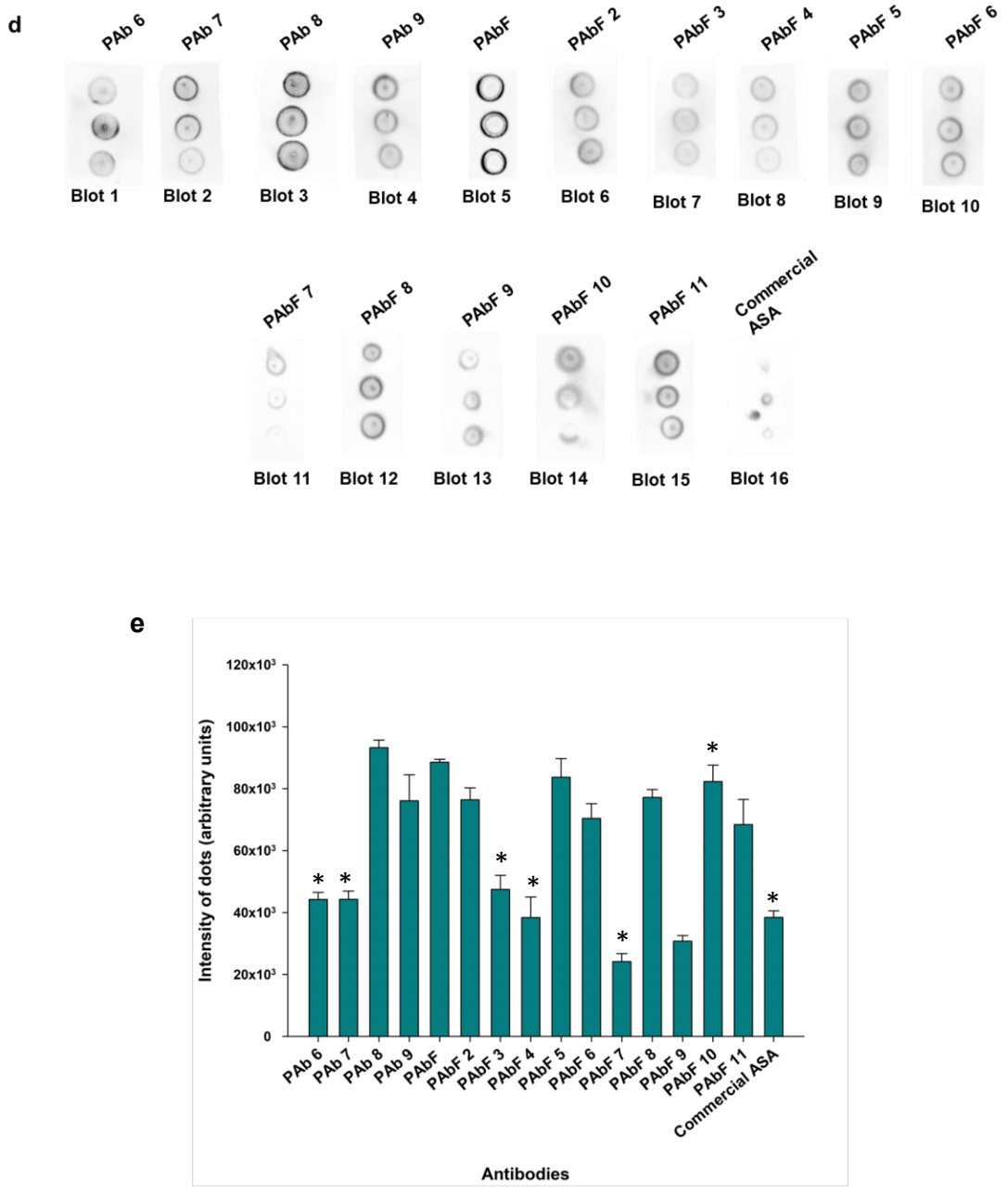

Fig. 5.2 (d) Dot blot assay to determine immune-recognition of PAbs (individual PAb 1, 2, 3, 4, PAbF, PAbF 2, 3, 4, 5, 6, 7, 8, 9, 10, and 11) using anti-rabbit IgG-HRP and commercial ASA using anti-horse IgG-HRP; **(e)** Dot intensities of the immune-recognition demonstrated by the secondary antibodies as stated in (d). Significance of

difference in immune-recognition of MTV by PAb 6,7, PAbF 3,4,7,10 and commercial ASA with respect to PAbF *p<0.05. Error bars indicate mean ± SD (n=3).

After normalising the dot intensities against the control without antigen intensities, we found the superior immune cross-reactivity of PAbF towards MTV spiked rat plasma compared to individual PAbs, PAb formulations and commercial ASA under similar experimental conditions (Fig. 5.2f, g).

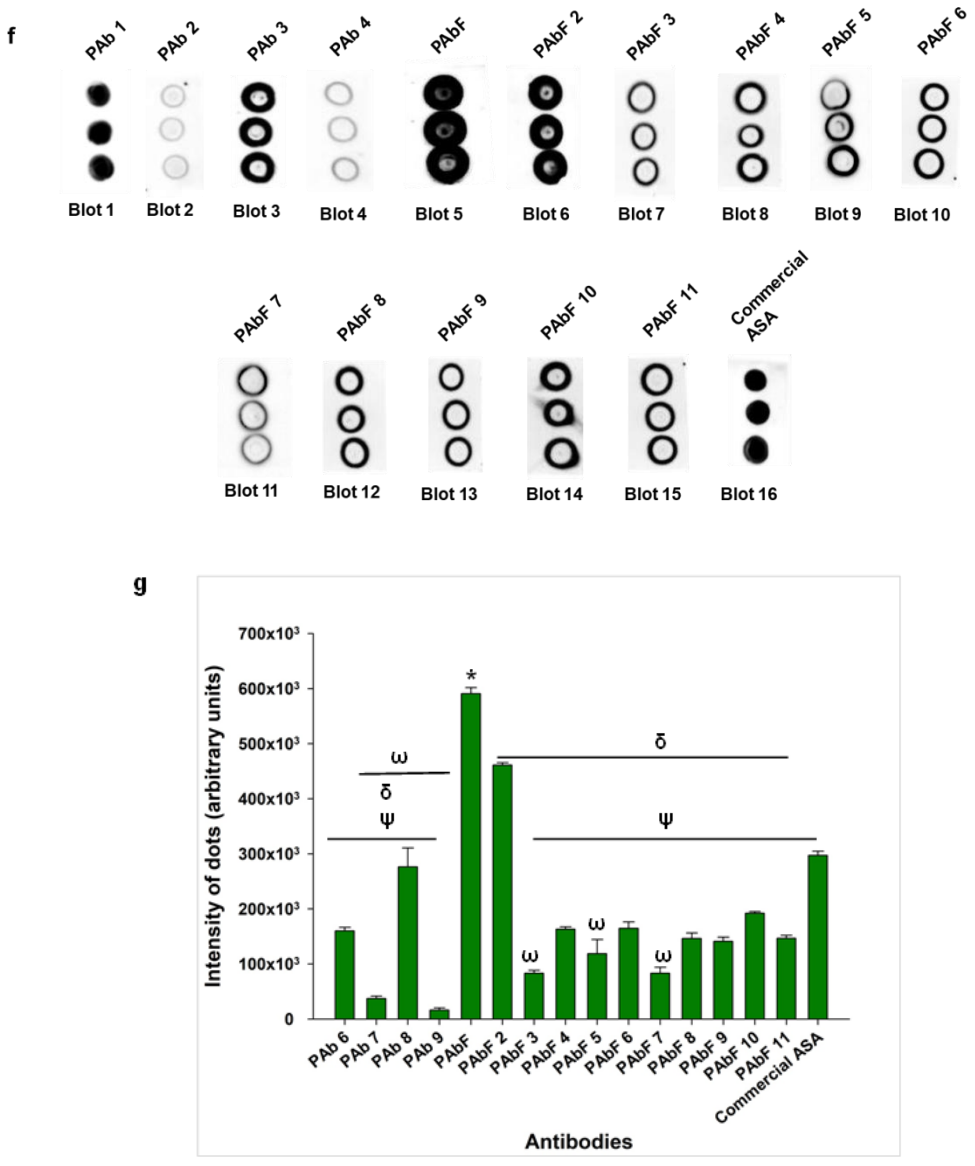

Fig. 5.2 (f) Dot blot assay of MTV (0.3 ng/µL) spiked rat plasma using the PAbs (individual PAb 1, 2, 3, and 4 and in combinations) and commercial ASA; **(g)** Image analyses of dot intensities of immune-reactivity determined as stated in (f). Significance

of difference of MTV immune-recognition by PAb individual and PAbF 2,3,4,5,6,7,8,9,10 and 11 compared to PAbF, *p<0.05; MTV immune-recognition by PAb individual and PAbF 2,3,4,5,6,7,8,9,10 and 11 compared to commercial ASA, $^{\delta}$p<0.05; MTV immune-recognition by PAb individual, PAbF 3,4,5,6,7,8,9,10 and 11 and commercial ASA compared to PAbF 2, $^{\Psi}$p<0.05; MTV immune-recognition by PAb 7,8,9 and PAbF 3, 5, 7 compared to PAbF 10, $^{\omega}$p<0.05. Error bars indicate mean ± S.D (n=3).

The dot blot analysis showed that PAbF could show excellent immune recognition of 0.3 ng/µL MTV spiked rat plasma and also an appreciable immune recognition of 0.15 ng/µL MTV spiked rat plasma; however, below this concentration of MTV, immune recognition was found to be non-existent after normalisation of the dot intensities measured (Fig. 5.2h, i).

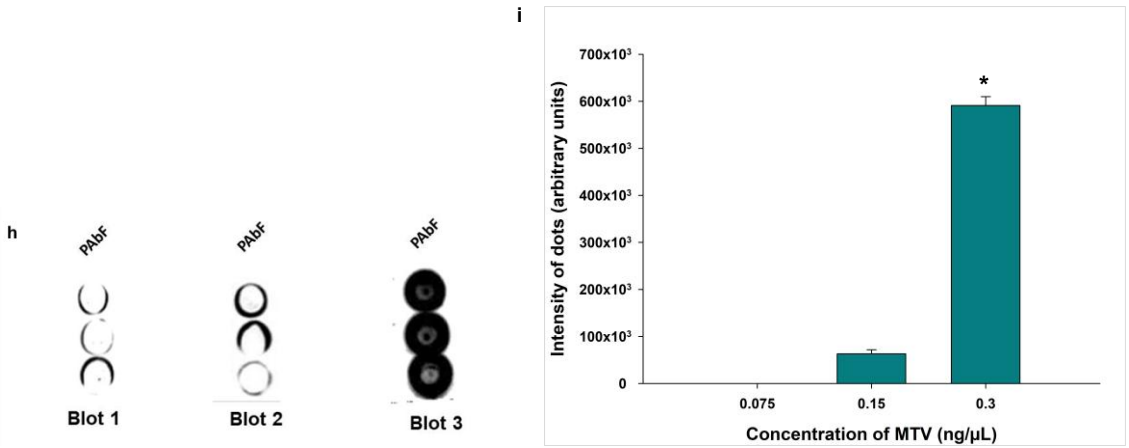

Fig. 5.2 (h) Dot blot assay of MTV (0.3 ng/µL, 0.15 ng/µL and 0.075 ng/µL) spiked rat plasma using the PAbF. Blot 1 was incubated with MTV (0.075 ng/µL) spiked rat plasma; Blot 2 was incubated with MTV (0.15 ng/µL) spiked rat plasma, and Blot 3 was incubated with MTV (0.3 ng/µL) spiked rat plasma; **(i)** Image analyses of dot intensities were performed using ImageJ software. The dot intensities have been normalised against intensities of control without antigen. Significance of difference of 0.15 ng/µL dose of MTV compared to 0.3 ng/µL dose of MTV *p<0.05. Error bars indicate mean ± S.D. (n=3).

The result of the western blot analysis also confirmed the better immune-recognition of the low molecular mass toxins of MTV by the PAbF as compared to recognition by commercial ASA (Fig. 5.2j-l).

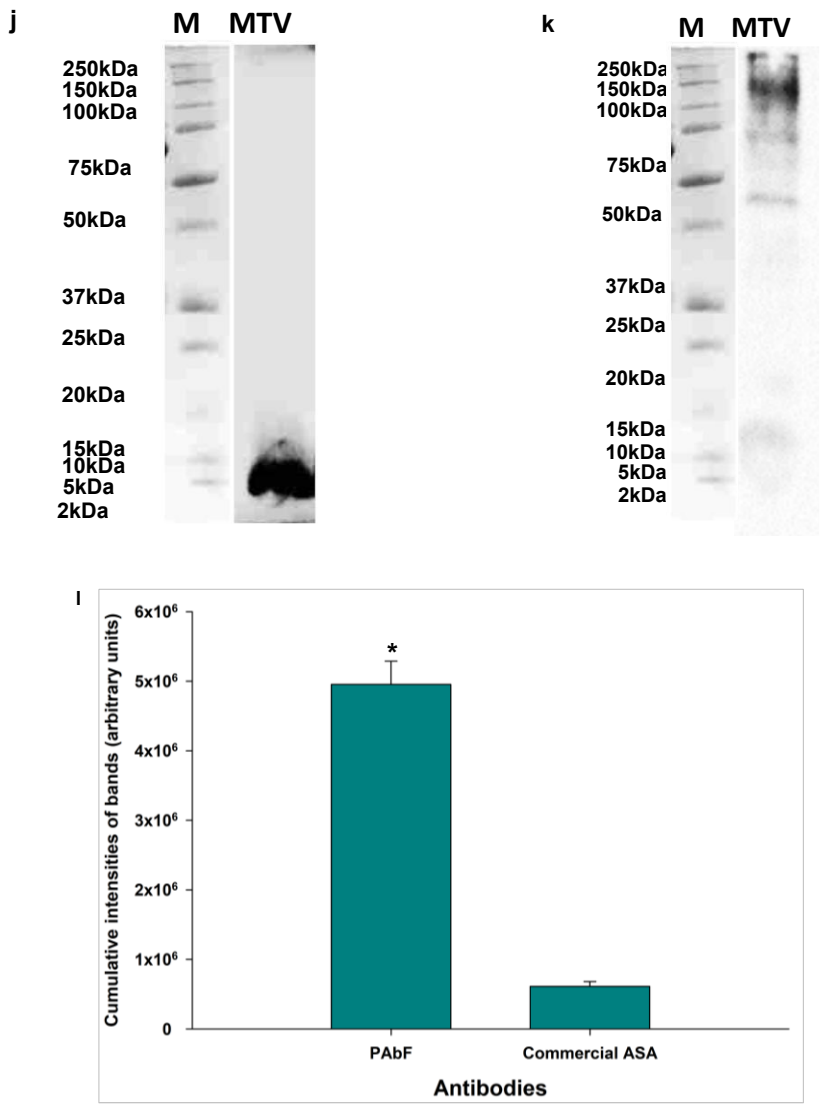

Fig. 5.2 (j) Western blot analysis to determine the immune recognition of MTV by PAbF. Immunoblot detected by HRP conjugated anti-rabbit IgG. **(k)** Western blot analysis to determine the immune recognition of MTV by commercial ASA. Immunoblot detected by HRP conjugated anti-horse IgG. Lane MTV represents the immunoblot of MTV, and lane M denotes the marker. **(l)** Densitometry analyses of the blot intensities of MTV detected by PAbF and commercial ASA. Significance of difference in recognition of the MTV by PAbF compared to recognition by commercial ASA, *$p<0.05$. Error bars indicate mean ± SD (n=3).

Through spectrofluorometric titration, the K_D value for PAbF was determined at 0.126 mg protein/mL (Fig. 5.2m), which was much lower than the K_D value of the commercial ASA (0.346 mg protein/mL) (Fig. 5.2m) under identical conditions.

m

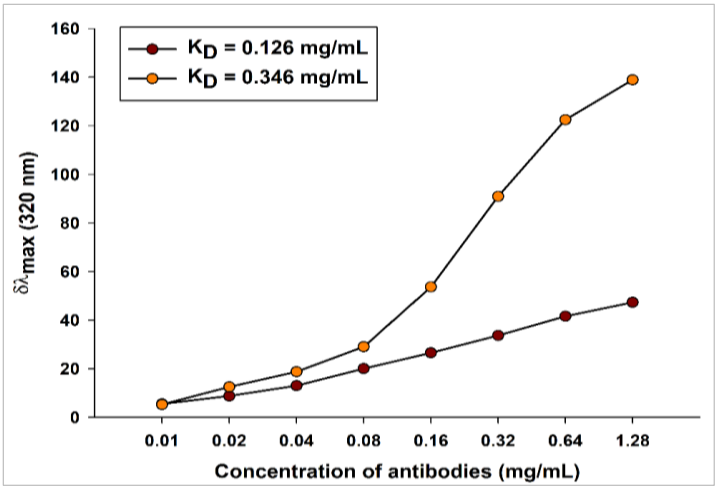

Fig. 5.2 (m) One-site specific binding curve representing spectrofluorometric interaction between a fixed concentration of MTV and graded concentrations of PAbF and commercial ASA (0.01 mg/mL, 0.02 mg/mL, 0.04 mg/mL, 0.08 mg/mL, 0.16 mg/mL, 0.32 mg/mL, 0.64 mg/mL, 1.28 mg/mL) showing the change in maximum fluorescence intensity (λ_{max}) of MTV-PAbF and MTV-commercial ASA binding with a fixed concentration of MTV. The graphs were plotted using GraphPad Prism 5.0 software and shows the mean of five scans.

5.1.3 The PAbF could better immune recognise the MTV enriched plasma sample compared to the non-enriched plasma sample from the envenomed Wistar rats

The dot blot analysis showed that PAbF detected the MTV in the plasma of the intravenously envenomed Wistar rats in a time-dependent manner; the highest recognition was shown 30 min and 60 min post-injection of MTV, and after that, the intensity of the signal (immune cross-reactivity between PAbF and MTV in plasma) decreased (Fig. 5.3 a,b). However, in the case of the subcutaneously envenomed Wistar rats, the immune recognition of MTV was found to increase from 30 min to 60 min and then decrease after 60 min (Fig. 5.3 a,b). Moreover, as expected, the PAbF showed much better recognition for MTV than the immunorecognition by commercial ASA (Fig. 5.3 a,b).

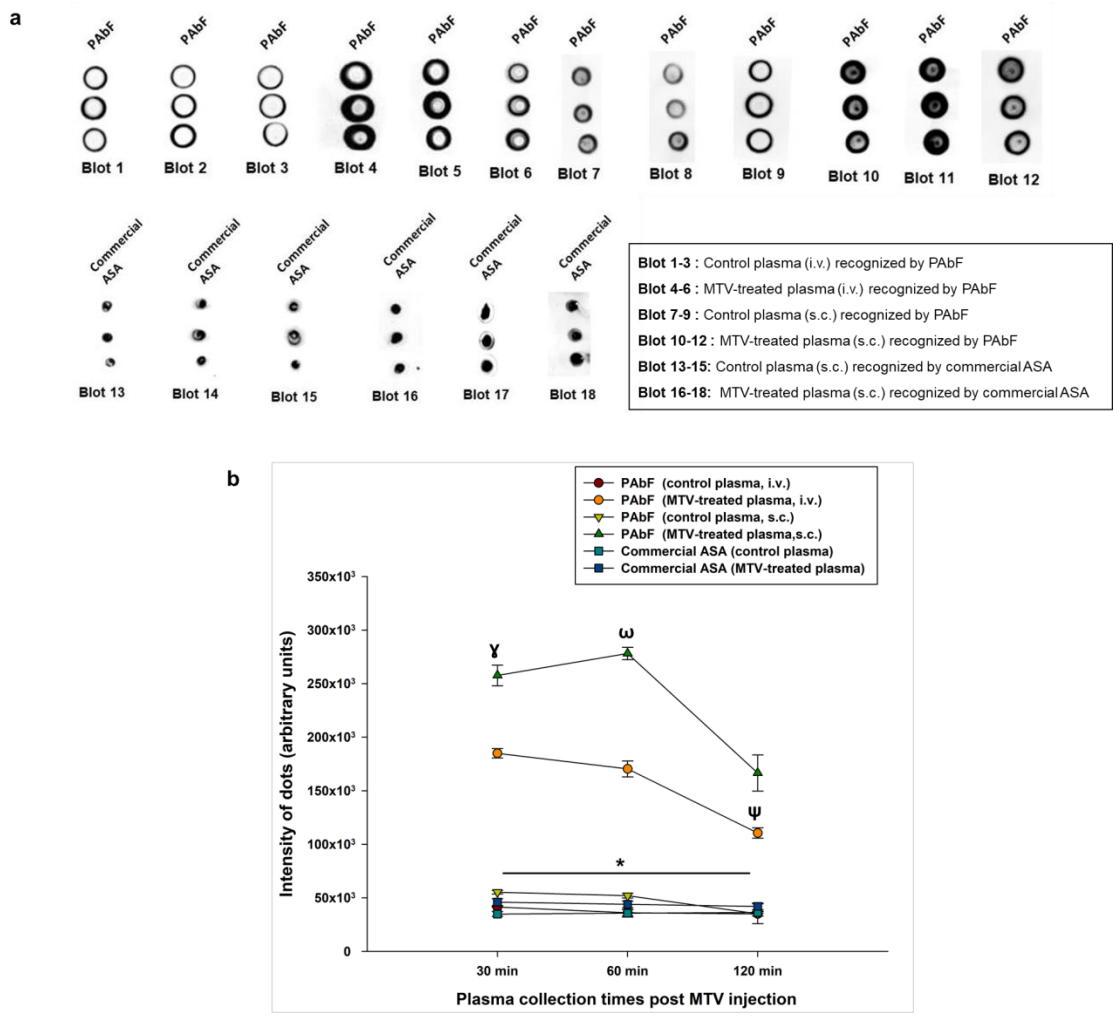

Fig. 5.3 (a) Dot blot assay comparing the immune-recognition of MTV in the plasma of the group I-IV rats by PAbF and commercial ASA when the blood was collected at 30 min, 60 min, and 120 min after the injection (i.v. and s.c.). Blots 1-3 incubated with control plasma (i.v.) collected after 30 min, 60 min, and 120 min recognised by PAbF; Blots 4-6 incubated with MTV-treated plasma (i.v.) collected after 30 min, 60 min, and 120 min recognised by PAbF; Blots 7-9 incubated with control plasma (s.c.) collected after 30 min, 60 min, and 120 min recognised by PAbF; Blots 10-12 incubated with MTV-treated plasma (s.c.) collected after 30 min, 60 min and 120 min recognised by PAbF; Blots 13-15 incubated with control plasma (s.c.) collected after 30 min, 60 min and 120 min recognised by commercial ASA; Blots 16-18 incubated with MTV-treated plasma (s.c.) collected after 30 min, 60 min and 120 min recognised by commercial ASA; **(b)** Image analyses of dot intensities of the group I-IV rats' plasma detection by PAbF and commercial ASA. The dot intensities have been normalised against intensities of control without antigen. Significance of difference in recognition of MTV-

treated plasma collected at 30 min, 60 min, and 120 min by PAbF compared to recognition by commercial ASA, *p<0.05; recognition of MTV-treated plasma (s.c.) collected at 60 min and 120min PAbF compared to recognition of MTV-treated plasma collected at 30 min, $^{\gamma}$p<0.05; recognition of MTV-treated plasma (s.c.) collected at 30 min and 120 min PAbF compared to recognition of MTV-treated plasma collected at 60 min, $^{\omega}$p<0.05; recognition of MTV-treated plasma (i.v.) collected at 30 min and 60 min by PAbF compared to recognition of MTV-treated plasma collected at 120 min, $^{\Psi}$p<0.05. Error bars indicate mean ± S.D. (n=3).

Dot blot analysis showed that the unique protocol developed in this study to enrich the envenomed plasma with low molecular mass MTV toxins is very potent (about 2 folds higher) in immune recognising the MTV in LMMPT-enriched MTV-treated plasma compared to the determination of MTV in non-enriched plasma (Fig. 5.3c, d). The sandwich ELISA also demonstrated MTV's superior immune recognition (about 2-fold higher) in LMMPT-enriched MTV-treated plasma compared to non-enriched MTV-treated plasma by PAbF (Fig. 5.3e).

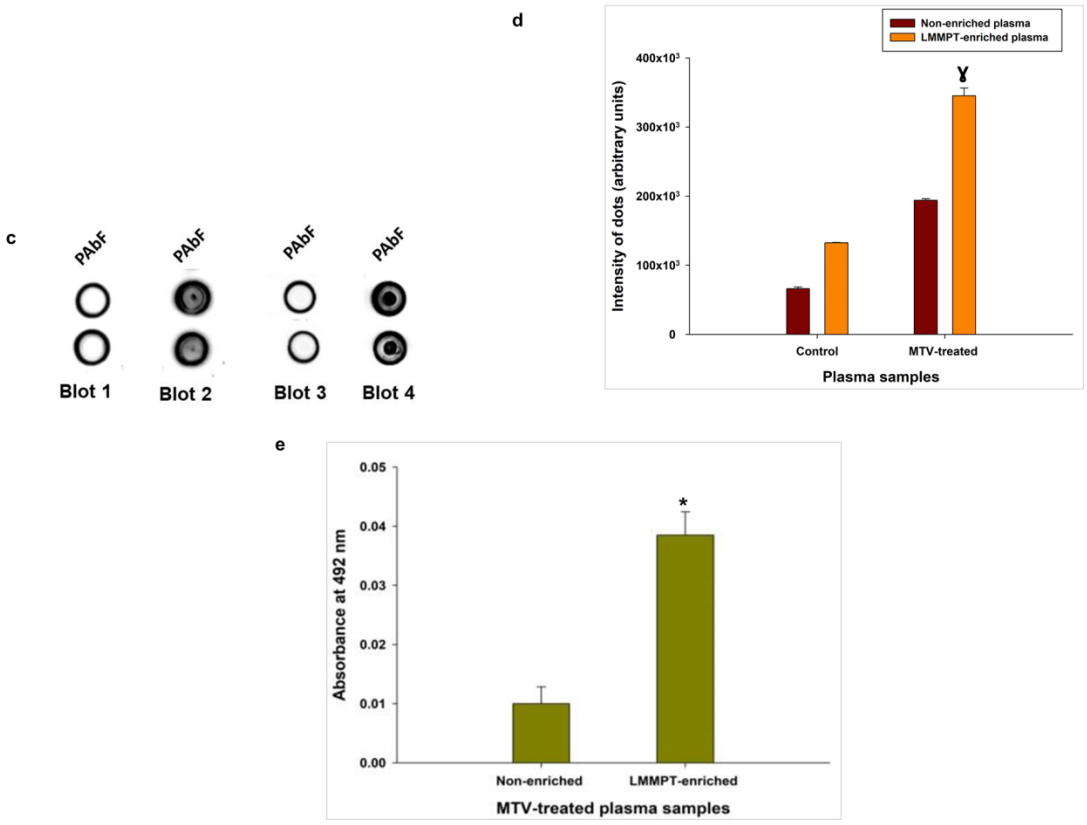

Fig. 5.3 (c) Comparison of immune cross-reactivity of PAbF towards MTV in the LMMPT-enriched MTV-treated and non-enriched plasma of envenomed rats. Blot 1

incubated with control non-enriched plasma; Blot 2 incubated with non-enriched MTV-treated plasma; Blot 3 incubated with control LMMPT-enriched MTV-treated plasma; Blot 4 incubated with LMMPT-enriched MTV-treated plasma; **(d)** Image analyses of dot intensities of the plasma detection by the PAbF. The dot intensities have been normalised against intensities of control without antigen. Significance of difference in recognition of LMMPT-enriched MTV-treated plasma compared to non-enriched MTV-treated plasma, $^{\gamma}p<0.05$; **(e)** Immune-reactivity of the PAbF towards MTV-treated non-enriched plasma and MTV-treated-LMMPT-enriched plasma determined by Sandwich ELISA. The absorbance values have been normalised against control without antigen. Significance of difference of recognition of MTV-treated-LMMPT-enriched plasma compared to MTV-treated non-enriched plasma, $^{*}p<0.05$. Error bars indicate mean ± S.D. (n=3).

5.1.4 Mass spectrometry analysis demonstrated the protocol developed in this study enriches the low molecular mass MTV toxins in MTV-treated rat plasma

The LC-MS/MS analysis of LMMPT-enriched MTV-treated rat plasma demonstrated the presence of scorpion venom K^+ and Na^+ channel toxins against the Buthidae family and *M. tamulus* databases. In contrast, these toxins could not be identified in control (untreated) plasma, which is obvious. In the MTV-treated rat plasma sample, the other protein identified against the Buthidae family and *M. tamulus* databases was the structural protein. The amino acid sequence alignment of the identified protein sequences with the K^+ and Na^+ channel toxins of MTV used for the custom peptide synthesis showed conserved residues of these toxins (Fig. 5.4).

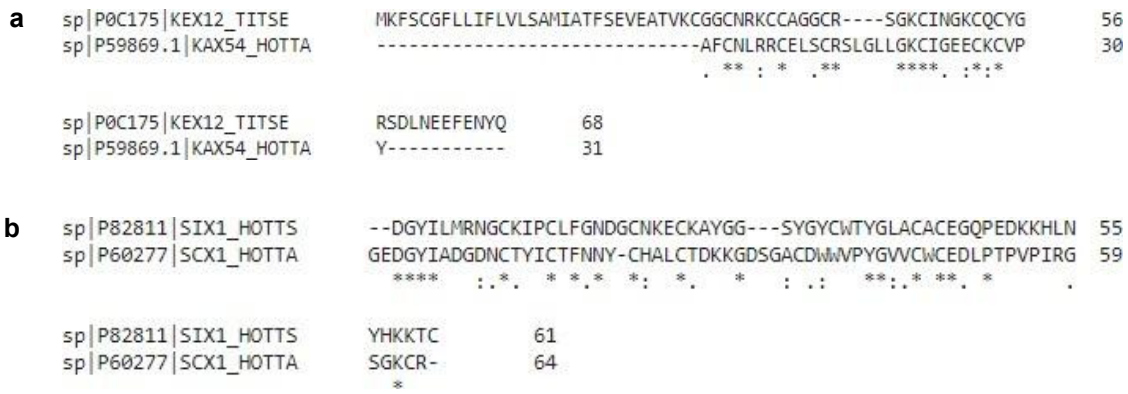

Fig. 5.4 Multiple sequence alignments of the **(a)** K^+ channel toxin, and **(b)** Na^+ channel toxin identified by LC-MS/MS analysis and the MTV K^+ and Na^+ channel toxin used for designing the custom peptides.

5.1.5 Biophysical characterisation demonstrated conjugation of PAbF with AuNPs

The synthesised AuNPs displayed a wine-red colour. The UV-Vis spectra recorded in the 400-700 nm range depicted a plasmonic peak at around 524 nm for the bare AuNPs. For antibody conjugation to the AuNPs, MUA functionalisation to the AuNPs showed a bathochromic shift of plasmonic peak from 524 nm to 528 nm. The peak showed a further bathochromic change to 530 nm after the conjugation of PAbF to the functionalised AuNPs (Fig. 5.5a).

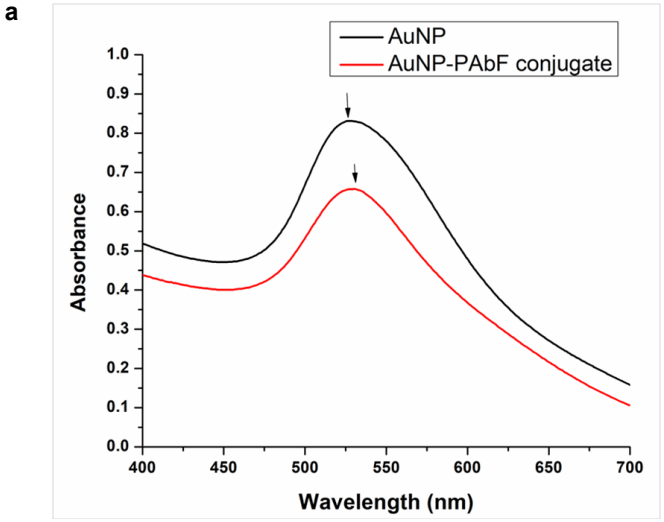

Fig. 5.5 (a) UV-Vis spectra of AuNP and AuNP conjugated with PAbF. The values are the mean of absorbance obtained in triplicates.

The infrared spectra of AuNP obtained from FTIR showed peaks at 3452 cm^{-1}, 2922 $cm^{-1,}$ and 1636 $cm^{-1,}$ characteristic of –O–H stretching, –C–H stretching, and –C=O stretching for the functional group of the citrate group stabilising the AuNPs [1-3]. When functionalized with MUA, peaks were observed at 2924 and 2854 $cm^{-1,}$ corresponding to symmetric and asymmetric -C-H elongation vibrations, respectively. Furthermore, the conjugation of the PAbF to functionalized AuNP resulted in a peak at 3433 $cm^{-1,}$ which represents amide NH_2 asymmetric stretching (3500 and 2800 cm^{-1}), another peak at 1644 cm^{-1}, which falls under the amide I region (1600-1700 cm^{-1}), and a broad band at 682 cm^{-1} for N–H wagging (750–650 cm^{-1}) [2-4](Fig. 5.5b). On the other hand, the zeta potential (mV) of the bare citrate-capped AuNPs and AuNP-PAbF conjugate was measured as −38.25 ± 0.07 mV and −30.31 ± 0.01 mV, respectively (Fig. 5.5c).

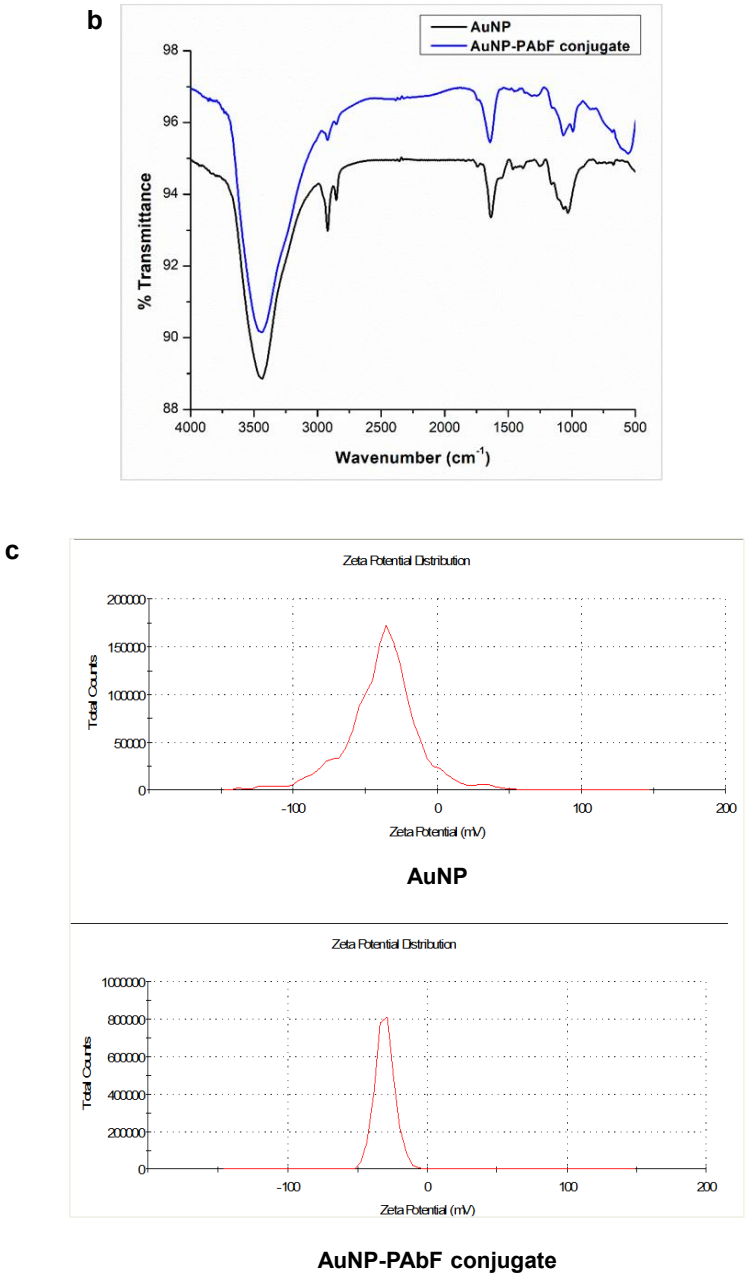

Fig. 5.5 (b) FTIR spectrum of AuNP and AuNP conjugated with PAbF; **(c)** Zeta potential of AuNP and AuNP conjugated with PAbF.

TEM analysis depicted monodisperse shapes for the bare citrate-capped AuNPs; however, when PAbF was conjugated to the AuNPs, the particles got aggregated (Fig. 5.5d, e). The particles' average diameter was 15.33 ± 0.12 nm and 16.44 ± 0.63 nm for bare AuNPs and AuNP-PAbF conjugate, respectively (Fig. 5.5f, g).

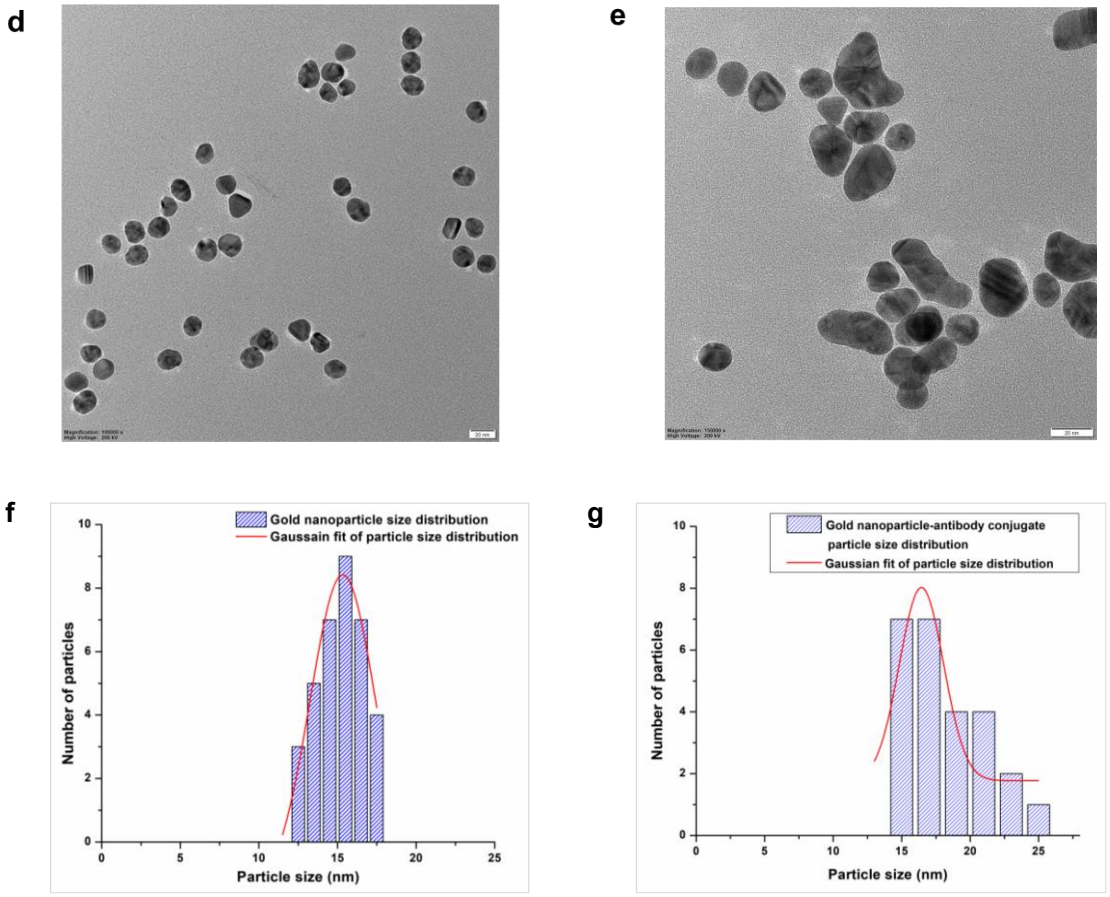

Fig. 5.5 TEM images of **(d)** AuNP and **(e)** AuNP-PAbF conjugate particle at 20 nm magnification; Particle size distribution histogram of **(f)** AuNP and **(g)** AuNP-PAbF conjugate particle in TEM images, with Gaussian function, fit using Originpro 8.5.

Further, the AFM analysis determined the height of the bare AuNP as 13.01 ± 0.03 nm, and after PAb adsorption, the size of the AuNP increased to 17.29 ± 0.17 nm (Fig. 5.5h-k).

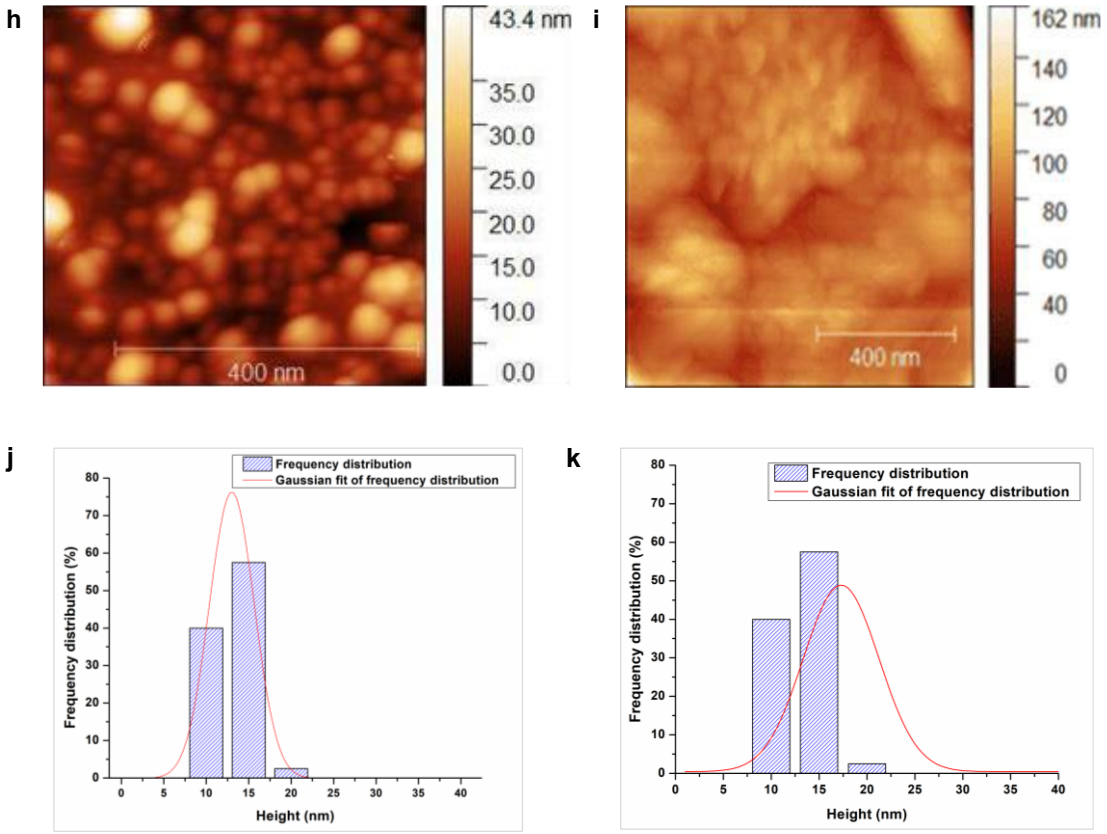

Fig. 5.5 Topographic 2D AFM images with scanned area 1000 x 1000 nm of **(h)** AuNP, **(i)** AuNP-PAbF conjugate; Histogram of height distribution of **(j)** AuNP, **(k)** AuNP-PAbF conjugate, from the topographic 2D AFM images with scanned area 1000 x 1000 nm.

The PAbF adsorption efficiency to the AuNP was 55.8 %, as determined via the calibrated Bradford protein assay curve (Fig. 5.5l).

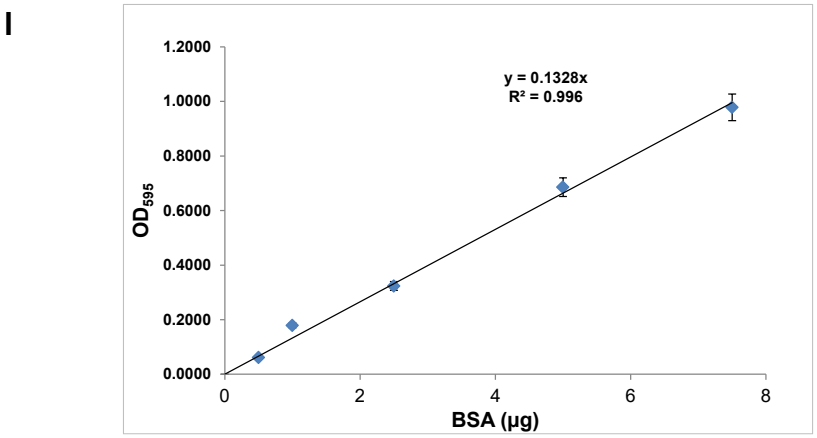

Fig. 5.5 (l) Calibration curve for estimating antibody (PAbF) left in the supernatant after conjugation to AuNP. Error bars indicate mean ± S.D. (n=3).

5.1.6 Detection of MTV in spiked serum (*in vitro*) and enriched plasma from envenomed Wistar strain rats (*in vivo*) by AuNP-PAbF conjugate and quantitation of MTV in envenomed plasma

The UV-Vis spectrum result suggests that under *in vitro* conditions, the AuNP-PAbF conjugate showed precise immune recognition of MTV spiked rat plasma (0.3 ng/µL); however, it did not show immune cross-reactivity towards negative controls NnV and RvV (Fig. 5.6a). For control, NnV, and RvV samples, the LSPR peak was observed at 530 nm. In contrast, for MTV, the peak shifted to 579 nm (Fig. 5.6a).

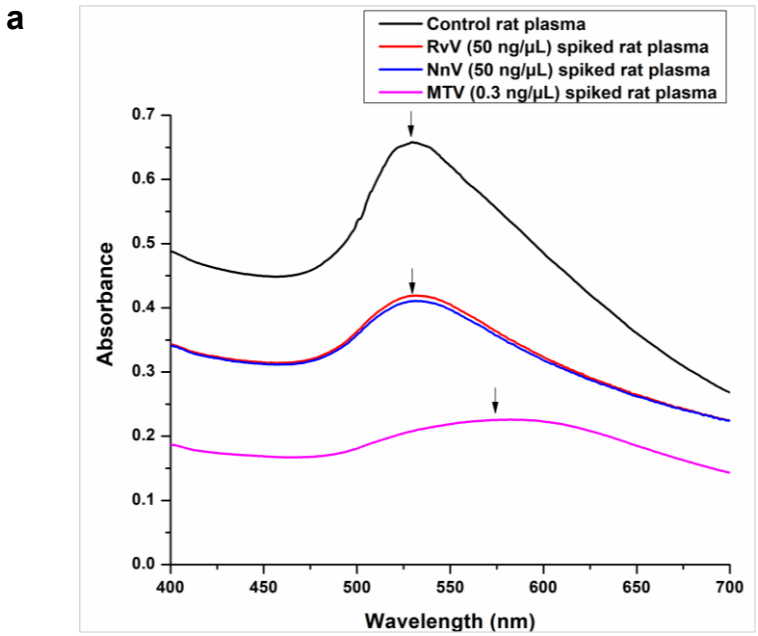

Fig. 5.6 (a) Absorbance spectra of the AuNP-PAbF conjugate in the presence of control (untreated rat plasma), MTV (0.3 ng/µL) spiked rat plasma, NnV, and RvV (50 ng/µL) spiked rat plasma. The values are the mean of absorbance obtained in triplicates.

In the case of LMMPT-enriched MTV-treated plasmas from groups III and IV rats, bathochromic shifts in absorption maxima (λ_{max}) from 530 nm of AuNP-PAbF conjugate to 538 nm were observed, suggesting the immunoreaction occurrence; however, no such wavelength shift or increase in absorption intensity was observed for control plasma from group I and III rats (Fig. 5.6b). The protocol developed in this study can rapidly detect MTV in the plasma of envenomed experimental rats within

5-10 min, indicating this method's suitability in the rural health centres for detecting MT envenomation.

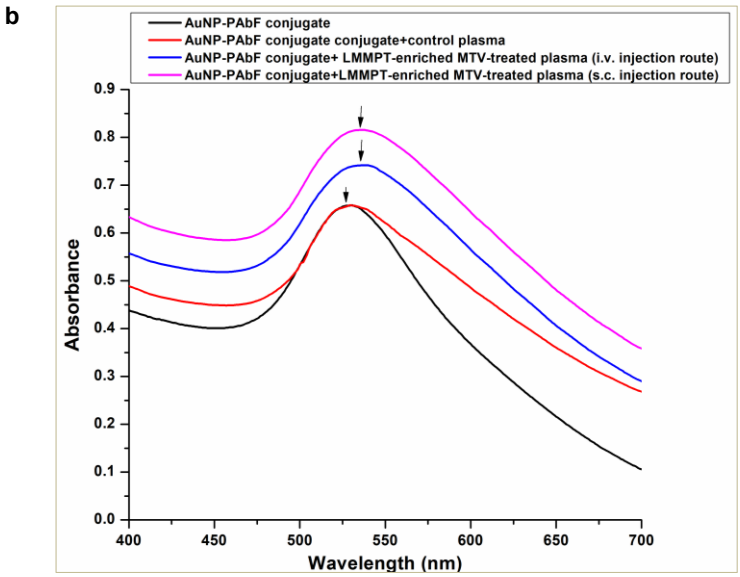

Fig.5.6 (b) Absorbance spectra of the AuNP-PAbF conjugate in the presence of control (untreated, group I and II) and MTV-treated-LMMPT-enriched plasma from group III and IV rats.

The AuNP-PAbF conjugate was treated with MTV concentrations ranging from 1 ng/µL to 5 ng/µL, and UV-Vis measurements were recorded. From Fig. 5.6c, it was observed that with an increase in MTV concentration, the characteristic peak of AuNPs at 524 nm decreased, and after aggregation of AuNPs, there was a shift in the band to around 540 nm. The MTV was quantified per previously available protocols [5,6]. The absorbance ratio of PAbF-venom aggregated peak to AuNP peak, i.e., A_{540}/A_{524}, was plotted against the concentration of MTV to obtain a calibration curve. It was found that A_{540}/A_{524} was proportional to the concentration of MTV with a regression coefficient R^2 = 0.9975 (Fig. 5.6d). The sensing method's detection limit (LoD) was calculated to be 0.3 ng/µL. The limit of quantitation (LoQ) was calculated to be 0.91 ng/µL as per the formula 10σ/S. By the above method, the venom quantity detected in the intravenously and subcutaneously injected LMMPT-enriched MTV-treated plasma was 0.64 ng/µL (38.8 ± 1.0%) and 3.05 ng/µL (48.3 ± 0.5%), respectively. Here, we would like to state that *in vitro* condition of venom detection differs from *in vivo* venom detection because several factors may interfere during *in vivo* venom detection.

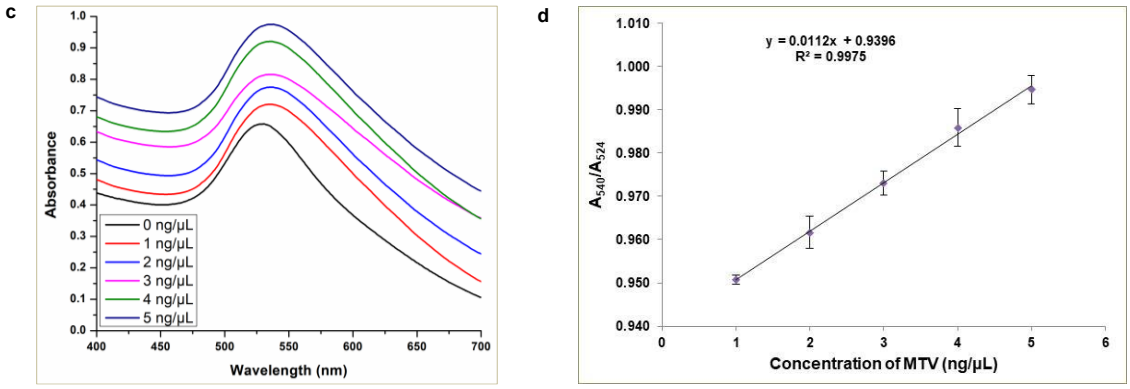

Fig. 5.6 (c) Absorbance spectrum for MTV spiked rat plasma detection. Absorbance curves correspond to plasma samples containing 1-5 ng/µL MTV; **(d)** Calibration curve for MTV spiked rat plasma detection at concentrations 1-5 ng/µL. Error bars indicate mean ± S.D. (n=3).

5.2 Discussion

Various clinical signs are documented in scorpion envenomation, and existing diagnostic methods reliant on these clinical manifestations may inadvertently jeopardize patients' health in cases of misdiagnosis. Consequently, employing this technique to verify noxious bites in clinical specimens with ambiguous diagnoses may prove beneficial. In recent years, synthetic peptides have garnered heightened scrutiny. Our work utilized their flexibility to generate polyclonal antibodies targeting the CPs unique to the MTV toxin epitope.

Obtaining scorpion venom is challenging since, after laborious procedures, only a minimal amount of venom can be extracted from each specimen, separating toxins from the entire venom complex. Additionally, purifying toxins is time-consuming, expensive, and yield-dependent. As a result, it is preferred to identify, design, and synthesise bespoke peptides because they can be produced consistently and with long-term stability. Additionally, synthetic peptides facilitate the measurement of antibodies specific to specific antigens, resulting in more precise assays [7,8].

Proteomic analysis of MTV revealed the predominance of low molecular mass K^+ and Na^+ channel toxins, accounting for 38.2% and 38.4% of the proteome, respectively [9]. The highest antigenic propensity epitopes of two major toxins of MTV viz. Na^+ and K^+ channel toxins were used to design the peptides that mimic the antigenic epitope of

these two major toxins of MTV to raise polyclonal antibodies against them. Since the rapid oxidation of cysteine residues in the native peptide sequence can affect peptide synthesis and purification by adversely influencing the cleavage of protecting groups [10], the cysteine residues were substituted with serine while designing toxin-epitope-specific custom peptides. There is very little difference between these two amino acids. Therefore, there are only minor differences in bond lengths and angles between these two amino acids, but the conversion of cysteine to serine can ease the peptide synthesis process [11]. Usually, the small size of peptides does not induce an immune response to produce high-titre antibodies in host animals [12]. Thus, the peptides were conjugated with carrier protein KLH via a bifunctional linker to raise a high titre of PAbs in rabbits [13,14].

Animal models have significantly contributed to advancing biomedical research by helping us understand various biological and pathological processes [15]. Due to their physiological similarity to humans, rodents have recently become the most commonly used species in biomedical research [16,17]. Their use can advance our understanding of various processes, including therapeutics, diagnostic methods, and biological development [15-17].

Detection at the concentration of 0.15 ng/µL may be beneficial to determine MTV in the plasma/serum of envenomed animals or humans, as reports have suggested that the maximum venom volume injected per sting of *M. tamulus* is 1.5 mg in approximately 5L of blood for an adult human (concentration of 0.3 ng/µL). Interestingly, PAbF showed synergistic action in significantly higher immune recognition of MTV than the individual PAbs. Such synergistic action of PAbs for MTV detection or any other venom protein detection has yet to be reported.

Moreover, a higher proportion of Na^+ and K^+ channel-specific antibodies in the PAbF showed significantly higher potency in immune recognition of MTV than commercial ASAs under identical experimental conditions. Furthermore, PAbF did not show immune cross-reactivity towards the snake venoms tested, ruling out that they could give false positive results against neurotoxic snakebites. Based on the results of the immune cross-reactivity of individual PAbs and PAbF with MTV as demonstrated by ELISA and dot blot assay, PAbF was used further to detect MTV in the plasma of envenomed rats.

The pharmacokinetics studies of other scorpion venoms (*A. australis garzonii*, *T. serrulatus,* and *B. occitanus tunetanus*) in rodents have demonstrated that the peak concentration of venom reaches in blood between 30 and 60 min after venom injection, and after that, the venom is distributed in the organs and eliminated rapidly from the blood [18-20]. Our latest study on the blood glucose levels in rats after MTV treatment has reported a significant increase in the levels 30 to 120 min post venom injection [21], and the finding of this study is in close agreement with these reports. Additionally, the signal intensity (immune cross-reactivity between PAbF and MTV in plasma) for the subcutaneously envenomed animal was higher than intravenously envenomed, which may be because more venom was injected via the subcutaneous route. Since the venom reaches blood at a slower rate via this route, the dispersion of venom from the bloodstream is slower than intravenous administration of MTV.

One of the mandates of our study was to develop a sensitive method that can detect a low concentration of MTV in the plasma of envenomed patients. However, the low molecular mass MTV toxins (or other peptides) in plasma are often veiled by the presence of high-abundance proteins (HAPs), which comprise more than 99% of the amount of protein in plasma [22,23]; consequently, it was an obstacle in our intention of developing of a sensitive kit for MTV detection. To overcome this problem, we developed a new technique to enrich LMMPT in MTV-envenomed plasma to detect scorpion envenomation better. The PAbF showed better immune recognition of MTV in LMMPT-enriched MTV-treated plasma than non-enriched MTV-treated plasma, thereby indicating that this technique can be helpful for the development of a sensitive, cost-effective, and rapid method for diagnosing and quantifying MTV in scorpion sting patients.

In snake and scorpion envenomation cases, there is often a considerable time gap between bite incidence and the arrival of most patients at health centres [19,24-26]. Since venom detection after a certain time interval post-sting is a difficult task due to the fast elimination of the venom, one of the objectives of this study was to develop a simple method that a technician can use in rural tropical primary and secondary health centres without the requirement of costly equipment for rapid diagnosis of scorpion envenomation. Immune-recognition techniques such as ELISA and western blot based on expensive chemicals and instruments may serve a different purpose. Therefore, we

considered developing a rapid and straightforward visual detection method for MTV envenomation. During the last couple of decades, AuNPs have shown tremendous promise in detecting biomaterials and various other applications [27-30].

AuNPs possess tuneable and unique optical properties due to the possession of a physical phenomenon called surface plasmon resonance (SPR). AuNPs strongly absorbed in the visible light region, and the light's oscillating electromagnetic field causes the conduction band electrons on the nanoparticle surface to collectively oscillate coherently [27,31]. The detection sensitivity by AuNP also depends on the size of the particle. There have been reports that AuNPs with larger sizes have better sensitivity but are not as stable as AuNPs of approximately 13-20 nm size [32,33].

In our study, the synthesised AuNPs were monodisperse with a size of around 13-15 nm, and the size of the AuNP-PAbFs increased marginally (16-17 nm). The amide bonds observed in the infrared spectroscopic studies confirmed the conjugation and the increase in zeta potential when compared to bare AuNPs. Because NaCl concentration plays a vital role in choosing the minimum concentration of PAbF required for stabilising the AuNP- PAbF complex, its optimum concentration was studied. NaCl aggregates AuNPs, changing the colour of the AuNP colloidal solution from red wine to purple/blue. The optimum binding concentration of PAbF to AuNPs surface to maintain the uniform dispersion was determined at 1 µg/µL, which is good enough to determine the low concentration of MTV in a scorpion-envenomed plasma sample. Furthermore, the AuNPs utilised in this study could be substituted with more sensitive detection systems, such as AuNP-coupled semiconductor quantum dots or fluorophore dyes, to increase the detection limit of MTV. However, the significant advantage of this protocol developed in this study is that it can rapidly detect MTV in the plasma of envenomed experimental rats within 5-10 min, indicating this method's suitability in the rural health centres for detecting MT envenomation.

The detection method proposed in our study necessitates using a visible range spectrophotometer to detect the LSPR peak shifting. The detection method may help quantify the circulating venom and assess the antivenom required to eliminate the venom from the blood. There have been a few reports of venom detection of scorpion species that are not endemic to India [34,35]. This paper presents the first analytical approach employing species-specific antibodies for the sensitive detection of MTV within 5-10

minutes. This approach serves as a proof-of-concept, necessitating more research to enhance the technique's sensitivity concerning nanoparticle conjugates. In the future, it may be possible to develop devices or kits utilizing image analysis, microfluidics, or lateral flow assays to detect MTV at the point of care quickly. Furthermore, a comprehensive examination of samples from a substantial cohort of patients stung by *M. tamulus* must be conducted to apply the suggested diagnostic approach in clinical settings.

Bibliography:

[1] Vechia, I. C. D., Steiner, B. T., Freitas, M. L., dos Santos Pedroso Fidelis, G., Galvani, N. C., Ronchi, J. M., Possato, J. C., Fagundes, M. Í., Rigo, F. K., and Feuser, P. E. Comparative cytotoxic effect of citrate-capped gold nanoparticles with different sizes on noncancerous and cancerous cell lines. *J Nanoparticle Res*, 22: 1-11, 2020.

[2] Stuart, B. H. *Infrared spectroscopy: fundamentals and applications*. John Wiley & Sons, England, 1-221, 2004.

[3] Pramanik, A., Gao, Y., Patibandla, S., Mitra, D., McCandless, M. G., Fassero, L. A., Gates, K., Tandon, R., and Ray, P. C. The rapid diagnosis and effective inhibition of coronavirus using spike antibody attached gold nanoparticles. *Nanoscale Adv*, 3(6): 1588-1596, 2021.

[4] Ji, Y., Yang, X., Ji, Z., Zhu, L., Ma, N., Chen, D., Jia, X., Tang, J., and Cao, Y. DFT-calculated IR spectrum amide I, II, and III band contributions of N-methylacetamide fine components. *ACS omega*, 5(15): 8572-8578, 2020.

[5] Bala, R., Kumar, M., Bansal, K., Sharma, R. K., and Wangoo, N. Ultrasensitive aptamer biosensor for malathion detection based on cationic polymer and gold nanoparticles. *Biosens. Bioel.*, 85: 445-449, 2016.

[6] Sittiwong, J. and Unob, F. Detection of urinary creatinine using gold nanoparticles after solid phase extraction. *Spectrochim Acta A Mol Biomol Spectrosc*, 138: 381-386, 2015.

[7] Puzari, U., Goswami, M., Rani, K., Patra, A., and Mukherjee, A. K. Computational and in vitro analyses to identify the anticoagulant regions of Echicetin, a snake venom anticoagulant C-type lectin (snaclec): possibility to develop anticoagulant peptide therapeutics? *J. Biomol. Struct. Dyn.*: 1-15, 2023.

[8] Meloen, R., Langedijk, J., and Langeveld, J. Synthetic peptides for diagnostic use. *Vet. Q*, 19(3): 122-126, 1997.

[9] Das, B., Patra, A., and Mukherjee, A. K. Correlation of venom toxinome composition of Indian red scorpion (*Mesobuthus tamulus*) with clinical manifestations of scorpion stings: failure of commercial antivenom to immune-recognize the abundance of low molecular mass toxins of this venom. *J. Proteome Res.*, 19(4): 1847-1856, 2020.

[10] Spears, R. J., McMahon, C., and Chudasama, V. Cysteine protecting groups: Applications in peptide and protein science. *Chem. Soc. Rev.*, 50(19): 11098-11155, 2021.

[11] Catalano, C., Mughram, M. H. A., Guo, Y., and Kellogg, G. E. 3D interaction homology: Hydropathic interaction environments of serine and cysteine are strikingly different and their roles adapt in membrane proteins. *Curr. Res. Struc. Biol.*, 3: 239-256, 2021.

[12] Hermanson, G. T. Preparation of hapten-carrier immunogen conjugates. In, *Bioconjugate Techniques*, of, pages 743-782. Academic Press, New York, 2008.

[13] Houen, G., Olsen, D., Hansen, P., Petersen, K., and Barkholt, V. Preparation of bioconjugates by solid-phase conjugation to ion exchange matrix-adsorbed carrier proteins. *Bioconj. Chem.*, 14(1): 75-79, 2003.

[14] Schaaper, W., Lankhof, H., Puijk, W., and Meloen, R. Manipulation of antipeptide immune response by varying the coupling of the peptide with the carrier protein. *Mol. Immunol.*, 26(1): 81-85, 1989.

[15] Domínguez-Oliva, A., Hernández-Ávalos, I., Martínez-Burnes, J., Olmos-Hernández, A., Verduzco-Mendoza, A., and Mota-Rojas, D. The importance of animal models in biomedical research: current insights and applications. *Animals*, 13(7): 1223, 2023.

[16] Makowska, I. J. and Weary, D. M. A good life for laboratory rodents? *ILAR journal*, 60(3): 373-388, 2019.

[17] Carbone, L. Estimating mouse and rat use in American laboratories by extrapolation from Animal Welfare Act-regulated species. *Sci Rep*, 11(1): 493, 2021.

[18] Revelo, M. P., Bambirra, E. A., Ferreira, A. P., Diniz, C. R., and Chávez-Olórtegui, C. Body distribution of *Tityus serrulatus* scorpion venom in mice and effects of scorpion antivenom. *Toxicon*, 34(10): 1119-1125, 1996.

[19] Krifi, M. N., Miled, K., Abderrazek, M., and El Ayeb, M. Effects of antivenom on *Buthus occitanus tunetanus* (Bot) scorpion venom pharmacokinetics: towards an optimization of antivenom immunotherapy in a rabbit model. *Toxicon*, 39(9): 1317-1326, 2001.

[20] Krifi, M. N., Savin, S., Debray, M., Bon, C., El Ayeb, M., and Choumet, V. Pharmacokinetic studies of scorpion venom before and after antivenom immunotherapy. *Toxicon*, 45(2): 187-198, 2005.

[21] Das, B., Madhubala, D., Mahanta, S., Patra, A., Puzari, U., Khan, M. R., and Mukherjee, A. K. A Novel Therapeutic Formulation for the Improved Treatment of Indian Red Scorpion (*Mesobuthus tamulus*) Venom-Induced Toxicity-Tested in Caenorhabditis elegans and Rodent Models. *Toxins*, 15(8): 504, 2023.

[22] Polaskova, V., Kapur, A., Khan, A., Molloy, M. P., and Baker, M. S. High-abundance protein depletion: comparison of methods for human plasma biomarker discovery. *Electrophoresis*, 31(3): 471-482, 2010.

[23] Righetti, P. G., Castagna, A., Antonucci, F., Piubelli, C., Cecconi, D., Campostrini, N., Rustichelli, C., Antonioli, P., Zanusso, G., and Monaco, S. Proteome analysis in the clinical chemistry laboratory: myth or reality? *Clin. Chim. Acta*, 357(2): 123-139, 2005.

[24] Das, B., Saviola, A. J., and Mukherjee, A. K. Biochemical and proteomic characterization, and pharmacological insights of Indian red scorpion venom toxins. *Front. Pharmacol.* , 12: 710680, 2021.

[25] Puzari, U. and Mukherjee, A. K. Recent developments in diagnostic tools and bioanalytical methods for analysis of snake venom: A critical review. *Anal. Chim. Acta*, 1137: 208-224, 2020.

[26] Selvanayagam, Z. E. and Gopalakrishnakone, P. Tests for detection of snake venoms, toxins and venom antibodies: review on recent trends (1987–1997). *Toxicon*, 37(4): 565-586, 1999.

[27] Ramalingam, V. Multifunctionality of gold nanoparticles: Plausible and convincing properties. *Adv. Colloid Interface Sci.*, 271: 101989, 2019.

[28] Chen, P. C., Mwakwari, S. C., and Oyelere, A. K. Gold nanoparticles: from nanomedicine to nanosensing. *Nanotechnol. Sci. Appl.*: 45-65, 2008.

[29] Li, W. and Chen, X. Gold nanoparticles for photoacoustic imaging. *Nanomedicine*, 10(2): 299-320, 2015.

[30] O'Neal, D. P., Hirsch, L. R., Halas, N. J., Payne, J. D., and West, J. L. Photo-thermal tumor ablation in mice using near infrared-absorbing nanoparticles. *Cancer Lett.*, 209(2): 171-176, 2004.

[31] Huang, X. and El-Sayed, M. A. Gold nanoparticles: Optical properties and implementations in cancer diagnosis and photothermal therapy. *J Adv. Res.*, 1(1): 13-28, 2010.

[32] Lou, S., Ye, J.-y., Li, K.-q., and Wu, A. A gold nanoparticle-based immunochromatographic assay: the influence of nanoparticulate size. *Analyst*, 137(5): 1174-1181, 2012.

[33] Guo, Y., Wang, Z., Qu, W., Shao, H., and Jiang, X. Colorimetric detection of mercury, lead and copper ions simultaneously using protein-functionalized gold nanoparticles. *Biosens. Bioelectron.*, 26(10): 4064-4069, 2011.

[34] Mars, A., Bouhaouala-Zahar, B., and Raouafi, N. Ultrasensitive sensing of *Androctonus australis hector* scorpion venom toxins in biological fluids using an electrochemical graphene quantum dots/nanobody-based platform. *Talanta*, 190: 182-187, 2018.

[35] Krifi, M. N., Kharrat, H., Zghal, K., Abdouli, M., Abroug, F., Bouchoucha, S., Dellagi, K., and El Ayeb, M. Development of an ELISA for the detection of scorpion venoms in sera of humans envenomed by *Androctonus australis garzonii* (Aag) and *Buthus occitanus tunetanus* (Bot): correlation with clinical severity of envenoming in Tunisia. *Toxicon*, 36(6): 887-900, 1998.